PAPER

Check for updates

3D printing of architected sulfur cathodes with dual-site atomic catalysts for accelerated polysulfide kinetics and Li-ion transport in high areal-loading lithium–sulfur batteries

Mahmoud M. Kaid, [a] Lineth Perez, [b] Shiraj Pokhrel, [a] Hong Zhao, [b] Shiyuan Zhou, [c] Gui-Liang Xu [c] and Hani M. El-Kaderi [*ad]

The practical deployment of lithium–sulfur batteries (LSBs) is hindered by fundamental limitations in conventional slurry-cast cathodes, including poor sulfur utilization, sluggish ion transport, and low areal capacity, particularly in thick electrodes required for high energy density. To address these challenges, we present direct ink writing (DIW) as an additive manufacturing strategy to fabricate advanced current-collector-free, 3D-printed sulfur cathodes (3DP S@CoNi-DSACs/NC) with hierarchically porous architectures that enhance lithium-ion diffusion, promote electrolyte penetration, and reduce interfacial resistance. The synergistic effects of Co/Ni dual-atom sites accelerate redox kinetics and mitigate polysulfide shuttling. As a result, the optimized 3DP cathode with a sulfur loading of 5.4 mg cm^{-2} demonstrated excellent rate capability, delivering a high reversible capacity of 1041.4 mAh g^{-1} at 1C with 85.5% capacity retention after 1000 cycles, significantly outperforming its cast counterpart. Remarkably, even at a higher sulfur loading of 8.1 mg cm^{-2}, the 3DP cathode maintains outstanding performance, achieving a discharge capacity of 1538.4 mAh g^{-1} and an areal capacity of 12.5 mAh cm^{-2} at 0.1C. This study not only demonstrates the functional integration of catalytically active materials into 3D printable sulfur cathode architectures but also offers a scalable and transformative platform for building high-performance LSBs beyond conventional electrode manufacturing methods.

Introduction

The limited energy density and high cost of conventional lithium-ion batteries (LIBs) present major challenges for long-range electric vehicles and grid-scale energy storage.[1] As a result, attention has shifted toward alternative battery technologies with higher capacities and improved sustainability.[2–5] Among these, lithium–sulfur batteries (LSBs) stand out due to their high theoretical energy density (~2600 Wh kg^{-1}), low cost, and the abundance of sulfur. The lithium anode offers a specific capacity of 3860 mAh g^{-1}, while sulfur undergoes a multi-electron conversion reaction, enabling 3–5 times the energy density of LIBs.[6] These advantages underscore the potential of LSBs as leading candidates for advanced energy storage solutions, especially in the context of renewable energy integration.

Despite their promise, the practical deployment of LSBs is limited by several challenges, including sluggish redox kinetics, lithium polysulfide (LiPS) shuttling, significant volume expansion (~80%) during sulfur conversion, and lithium dendrite formation.[7–10] These issues can cause cathode degradation, mechanical stress, and loss of electrical contact, ultimately reducing energy density and cycling stability. Addressing these barriers requires advanced materials design and manufacturing strategies to regulate lithium-ion transport and redox reactions. On the materials side, metal doping of sulfur hosts in the form of coordinated single atoms or supported nanoparticles (NPs) has shown great promise in maintaining high-capacity retention and excellent rate performance by alleviating the shuttle effect and enhancing catalytic activity.[11–14] Unlike nanoparticles, the single-atom catalysts (SACs) prevent metal agglomeration and offer high active site density. Apart from conventionally fully isolated SACs, dual single-atom catalysts DSACs enable tunable electronic structures through spatially correlated metal centers, which can significantly impact the sulfur redox reaction during the discharge/charge process.[15–17] These advances highlight the catalytic promise of DSACs, yet their integration into practical, high-loading electrodes remains largely unexplored.

[a]Department of Chemistry, Virginia Commonwealth University, Richmond, VA 23284, USA. E-mail: helkaderi@vcu.edu; Fax: +1(804) 828-8599

[b]Department of Mechanical & Nuclear Engineering, Virginia Commonwealth University, Richmond, VA 23284, USA

[c]Chemical Sciences and Engineering Division, Argonne National Laboratory, Lemont, IL 60439, USA

[d]Functional Materials Group, Gulf University for Science and Technology, Hawally 32093, Kuwait

This journal is © The Royal Society of Chemistry 2025

J. Mater. Chem. A, 2025, **13**, 38421–38435 | **38421**

On the manufacturing side, conventional slurry casting techniques are still the dominant method for cathode preparation. However, they involve toxic solvents such as *N*-methyl-2-pyrrolidone (NMP), waste heavy metal current collectors, high energy consumption, and produce planar electrodes with limited mass loading and poor design flexibility.[18,19] These constraints limit the translation of advanced chemistries, such as SACs/DSACs, into device-relevant, high-loading electrodes. This raises a central scientific question: how can catalytic sulfur hosts be incorporated into electrode architectures that simultaneously achieve high sulfur loading, efficient ion transport, and lean-electrolyte operation?.

Additive manufacturing, particularly direct ink writing (DIW), offers a promising platform to address this gap and provide a greener processing with reduced solvent toxicity and current collector waste.[20–22] Unlike slurry casting, DIW offers unprecedented design flexibility, enabling the creation of tailored 3D electrode architectures that enhance sulfur utilization, improve ion/electron transport, suppress polysulfide shuttling, and enhance mechanical robustness. Furthermore, DIW allows for precise ink deposition and direct printing onto diverse substrates, paving the way for integrated device configurations that are difficult to achieve with conventional coating. These structural and processing advantages make DIW a promising route for developing high-performance LSBs, even though large-scale throughput comparable to slurry casting remains a longer-term goal. Prior studies on 3D-configured electrodes in lithium-ion batteries confirm that "line" and "grid" architectures outperform planar designs in areal capacity, rate capability, and cycling stability due to improved charge distribution and shortened ion-diffusion pathways.[23] However, the application of DIW to sulfur cathodes under practical conditions of high areal loading and lean electrolyte remains underexplored.[24–26] Most importantly, the synergistic integration of DSAC chemistry with 3D-printed architectures in LSB cathodes has not been systematically investigated.

In this work, we address this gap by combining the catalytic activity of CoNi-DSACs/NC with the structural control of DIW to develop high-loading, current-collector-free sulfur cathodes. This integrated materials-manufacturing strategy enables us to disentangle the roles of chemistry and architecture, and to evaluate how their combination impacts ion transport, redox kinetics, and ultimately device-level performance. Tailored ink formulations were developed to enable DIW fabrication of cathodes with practical sulfur loadings and controlled electrolyte-to-sulfur (E/S) ratios, two critical parameters for achieving high energy density. The resulting 3DP S@CoNi-DSACs/NC cathodes feature hierarchical micro/macroporous architectures that promote rapid lithium-ion diffusion, effective polysulfide confinement, and enhanced catalytic conversion *via* Co/Ni dual single-atom active sites. Coin cells incorporating the 3DP S@CoNi-DSACs/NC cathode with areal sulfur loading of 5.4 mg cm^{-2} exhibited excellent rate capability, achieving a specific capacity of 1567.3 mAh g^{-1} at 0.1C. Even when the sulfur loading increased to 8.1 mg cm^{-2}, the 3DP cathode displayed an outstanding areal capacity of 12.5 mAh cm^{-2} at 0.1C. Beyond electrochemical advantages, the 3D-printed designs eliminate the need for heavy metal current collectors, further improving the effective energy density. Taken together, this study establishes a synergistic approach that integrates advanced catalytic chemistry with additive manufacturing, providing a model platform for next-generation, high-performance LSBs.

Results and discussion

Integrating highly active single atoms as a catalytic sulfur host with additive manufacturing of the electrodes enables rapid and cost-effective fabrication of stable high-energy-density LSBs. The catalytic sulfur host was designed by thermolysis of ZIF-L and post-synthesis metalation to create single-atom catalysts (SACs) and dual-single-atom catalysts (DSACs) supported on highly porous nitrogen-doped carbon, as schematically presented in Fig. 1a. ZIFs possess a unique structural trait wherein metal centers exclusively coordinate with nitrogen atoms of imidazolate linkers, forming an interconnected framework. Upon thermal activation, the metal coordination with nitrogen maintains the isolation of metal centers, facilitating the formation of SACs with uniform dispersion. The post-synthetic metalation method enabled control over catalyst loading level, dispersity, metal type, and composition.[27] In this process, an advanced two-step annealing technique was applied to produce SACs and DSACs with high metal content density (Co = 7.6 wt% and Ni = 7.4 wt%). This thermolysis approach offers the advantage of retaining a high metal surface coverage by selectively binding the metal to all available coordination sites. Any unbound species are subsequently removed through washing after the first-step pyrolysis, thereby preventing metal agglomeration during subsequent high-temperature steps. This method stabilizes significantly higher metal contents compared to traditional impregnation techniques. The elemental data obtained from ICP-MS and EDS analysis reveal an ultra-high density of metal content in the synthesized SACs/NC and DSACs/NC electrocatalysts, as summarized in Table S1.

Scanning electron microscopy (SEM) images of the nitrogen-doped carbon (NC) matrix and CoNi-DSACs/NC displayed exfoliated two-dimensional sheets for NC derived from ZIF-L, as illustrated in Fig. 1 and S2. The images show a uniform distribution of NC sheets, which contributes to improved electron transport and the creation of microscopic pores for storing sulfur through interconnected with one another. More importantly, these images confirmed that the metalation of NC *via* the two-step pyrolysis process prevents the aggregation of cobalt/nickel single atoms into nanoparticles. The high density of the synthesized DSACs was further elucidated through aberration-corrected high-angle annular dark-field scanning transmission electron microscopy (HAADF-STEM) to analyze the spatial distribution of cobalt and nickel within the NC matrix. As shown in Fig. 1e–g, the HAADF-STEM images reveal atomically dispersed Co and Ni sites (~0.1 nm) embedded in the amorphous NC support. The presence and uniform distribution of these metals are further confirmed by the EDS elemental mapping shown in Fig. 2i–l. In addition, SI Video 1 provides dynamic confirmation of these atomically dispersed Ni

38422 | *J. Mater. Chem. A*, 2025, **13**, 38421–38435

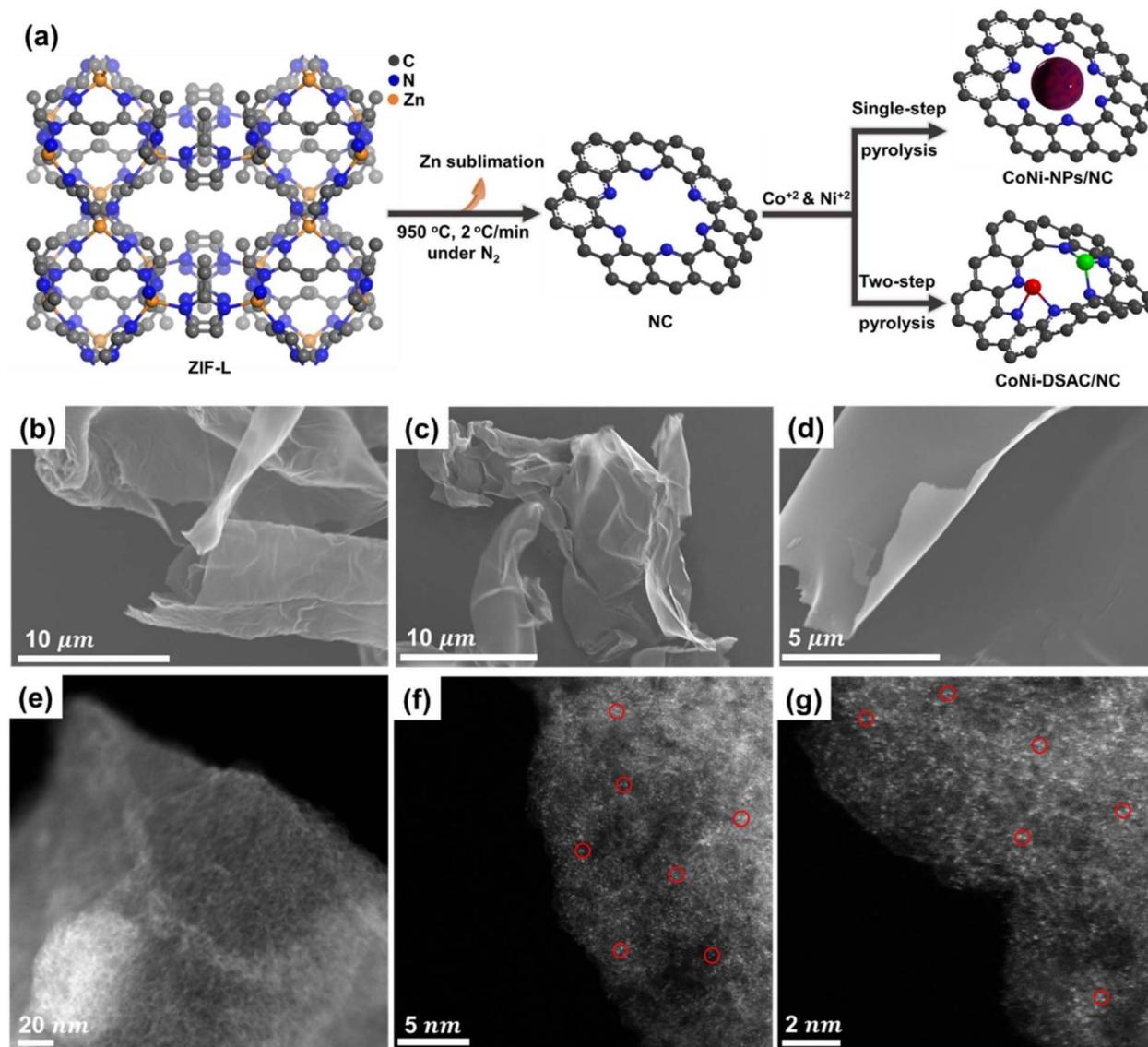This journal is © The Royal Society of Chemistry 2025

Fig. 1 Synthetic process and material characterization. (a) Schematic illustration of the synthesis of CoNi-DSACs/NC and CoNi-NPs/NC as electrocatalytic sulfur hosts. SEM images of (b) NC derived from ZIF-L and (c and d) CoNi-DSACs/NC. (e–g) HAADF-STEM images of CoNi-DSACs/NC, where the bright spots correspond to atomically dispersed Ni and Co single atoms (representative sites are highlighted with red circles for clarity).

and Co sites, further supporting their homogeneous distribution within the NC framework. The precise positioning of Co and Ni within the NC highlights the effectiveness of the synthetic strategy in achieving a well-defined dual-metal architecture without significant aggregation. This well-defined distribution is crucial for enhancing sulfur-based cathodes in LSBs, as the Co/Ni dual sites and NC host synergistically regulate polysulfide redox reactions, mitigate the shuttle effect, and improve sulfur utilization. Additionally, the high-density architecture of the DSACs ensures robust electrical conductivity, further contributing to the overall electrochemical performance of LSBs.

Powder X-ray diffraction peaks for CoNi-NPs/NC and CoNi-DSACs/NC provide additional evidence of the significance of the two-step pyrolysis technique in producing ultra-high-

density single atoms, as illustrated in Fig. 2a. In the case of CoNi-NPs/NC (single-step pyrolysis), the two distinct peaks at 2θ = 44.43 and 51.91° correspond to the (111) and (200) planes of the face-centered cubic (fcc) phase of Co/Ni-NPs.[11,28] Conversely, the XRD pattern of CoNi-DSACs/NC (two-step pyrolysis) does not reveal any characteristic peaks of Co/Ni crystals, indicating that Co and Ni are present as single atoms in the case of the two-step pyrolysis technique. It is essential to note that, despite employing the two-step pyrolysis technique, the presence of small Co/Ni crystals was observed when the metal loading exceeded 15 wt%. To assess the effectiveness of single atoms in LSBs, 80 wt% of elemental sulfur was melt-diffused at 155 °C under vacuum over different hosts (NC, Co-SACs/NC, Ni-SACs/NC, and CoNi-DSACs/NC) for battery studies. As depicted in Fig. 2b, all XRD peaks can be well-assigned to sulfur (PDF#08-
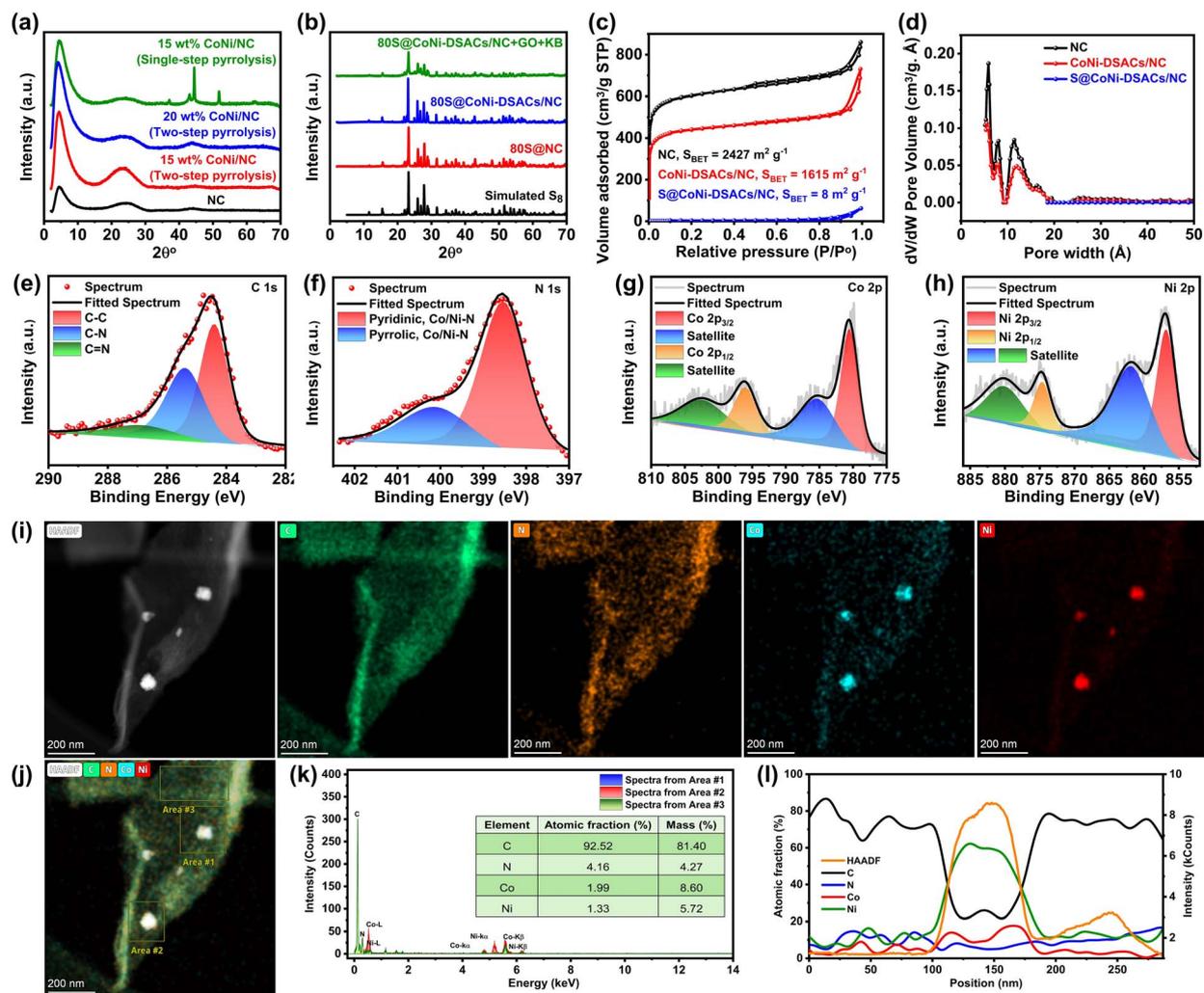
Fig. 2 (a and b) PXRD patterns of the prepared electrocatalytic sulfur hosts. (c) N$_2$ adsorption–desorption isotherm and (d) pore size distribution of NC, CoNi-DSACs/NC and S@CoNi-DSACs/NC utilizing non-local density functional theory (NLDFT). High-resolution XPS (e) C1s, (f) N 1s, (g) Co 2p, and (h) Ni 2p for CoNi-DSACs/NC. (i–l) EDS mapping of CoNi-DSACs/NC. Inset of (k): table summarizes the elemental mass% obtained based on Area#3 in (j). (l) The weight fraction % obtained based on Area #2 in (j).

0247), specifically prominent at about 23.12°, 25.80°, and 27.71°, which correspond to crystal planes of (222), (026), and (206), respectively.[29,30] The sulfur content of the prepared cathodes was investigated using TGA-MS analysis under N$_2$ atmosphere (Fig. S3). The analysis of S@CoNi-DSACs/NC revealed a sulfur content of 81 wt%, indicating that high sulfur loading can be effectively accommodated in the micropores of CoNi-DSACs/NC. In pursuing high areal energy density in LSBs, it is important to recognize the significant role of high sulfur content. However, it is commonly observed that high sulfur content alone may lead to reduced sulfur utilization unless catalysts are employed.[31]

The nitrogen adsorption–desorption isotherms were analyzed to assess the porosity of the NC, CoNi-DSACs/NC, and S@CoNi-DSACs/NC samples, as depicted in Fig. 2c. According to IUPAC classifications, these isotherms correspond to type IV, revealing the micro–mesoporous structure.[32] The NC, derived from the pyrolysis of ZIF-L intercalated with KCl, exhibited a BET surface area of 2427 m^2 g^{-1}. The specific surface area of

CoNi-DSACs/NC was measured to be 1615 m^2 g^{-1}, retaining roughly 66.5% of the original surface area of the NC sample. Pore size distribution analysis was conducted using non-local density functional theory (NLDFT), revealing that the majority of pores in the prepared samples are microporous, as illustrated in Fig. 2d. Such a highly porous morphology of CoNi-DSACs/NC substrate provides space for sulfur impregnation. Upon introducing 80 wt% sulfur onto the CoNi-DSACs/NC via the melt diffusion method, the nitrogen adsorption–desorption isotherm indicated the formation of a nonporous material. This observation suggests the complete saturation of the available pores within the CoNi-DSACs/NC framework with sulfur, effectively eliminating any porosity. The SEM images of 80 wt% S@CoNi-DSACs/NC reveal a smoother and more compact structure compared to the bare CoNi-DSACs/NC electrocatalyst (Fig. S4).

The chemical composition of NC and CoNi-DSACs/NC was examined by X-ray photoelectron spectroscopy (Fig. 2e–h and S5). The high-resolution C 1s spectrum of CoNi-DSACs/NC

38424 | J. Mater. Chem. A, 2025, 13, 38421–38435

This journal is © The Royal Society of Chemistry 2025

spectrum revealed three subpeaks (Fig. 2e). Peak 1, observed at 284.4 eV, corresponds to sp^2 carbon, while peaks 2 and 3 are attributed to carbon–nitrogen bonds (C–N and C=N) at 285.4 and 286.9 eV, respectively.[33–35] Crucially, N1s deconvolution reveals a pronounced redistribution of nitrogen species upon Co^{2+}/Ni^{2+} loading, where the pyridinic component shifts from 398.26 to 398.53 eV (+0.27 eV) with a large increase in relative area and peak intensity, while the pyrrolic component shifts slightly from 400.36 to 400.12 eV (−0.24 eV) and decreases from 67.2% to 28.2%. These spectral shifts, the change in relative intensities, and the pyridinic peak sharpening are indicative of the formation of a more uniform, metal-bound pyridinic N environment with some involvement of pyrrolic N.[36–39] Supporting metal core-level spectra show Co 2p features at 780.5 and 796.4 eV with satellites (784.5, 802.4 eV) and Ni 2p peaks at 856.8, 861.8, 874.6, and 880.1 eV, consistent with Co^{2+} and Ni^{2+} species coordinated to N and the absence of metallic Co/Ni (Fig. 2g and h).[40–42] Overall, the XPS data indicate that Co^{2+}/Ni^{2+} are present as atomically dispersed, nitrogen-coordinated species (Co–/Ni–N motifs) on NC, supporting the proposed DSAC structure.

To further verify the elemental composition and spatial distribution of Co and Ni within the NC framework, energy-dispersive X-ray spectroscopy (EDS) mapping was conducted. The EDS elemental maps distinctly showed the co-localization of cobalt and nickel, with both elements consistently distributed in close proximity across the NC framework, as shown in Fig. 2i. This near-uniform arrangement suggests a synergistic interaction between Co and Ni at the atomic level, likely facilitated by the nitrogen coordination sites, which could influence the local electronic structure and coordination environment. The dense distribution of these dual-metal sites within the NC framework indicates a highly controlled synthesis process, ensuring uniform metal incorporation without significant aggregation. Additionally, the quantitative analysis derived from the EDS spectra aligns with the targeted loading and confirms the ICP results, as shown in Fig. 2k and Table S1.

Battery performance

This study investigates how electrode manufacturing (slurry casting vs. DIW 3D printing) alters ion-diffusion dynamics, interfacial kinetics, the achievable areal capacity, and cell-level energy density of high-loading Li–S cathodes. To decouple chemistry from architecture, inks with identical catalyst and sulfur loadings were used to fabricate matched slurry-cast films and current-collector-free DIW-printed cathodes; all electrochemical comparisons were performed in Li–S coin cells under controlled conditions (see Experimental methods in the SI). The subsections below present coin-cell performance for cast and 3D-printed cathodes, along with a concise comparison that links manufacturing with transport/kinetics and practical performance.

Coin-cell performance of the cast cathodes

Cyclic voltammetry (CV) was performed on cast cathodes (80 wt% sulfur) to evaluate the electrocatalytic activity of various SACs in LSBs. In Fig. 3a, the two cathodic peaks represent the stepwise reduction of S_8 to long-chain Li_2x ($x = 4$–8), followed by further conversion to Li_2S_2/Li_2S. It is worth noting that a positive shift in reduction peaks indicates accelerated LiPS conversion and enhanced kinetics, while a negative shift in oxidation peaks suggests lower overpotential and improved charge transfer. Compared to NC, Co-SACs/NC exhibited a positive shift in reduction peaks, whereas Ni-SACs/NC showed a negative shift in oxidation peaks, demonstrating their individual catalytic roles. The CoNi-DSACs/NC cathode combines the advantages of both electrocatalysts, resulting in sharper redox peaks, higher current densities, and the lowest polarization potential (0.33 V) vs. 0.50, 0.41, and 0.39 V for NC, Co-SACs/NC, and Ni-SACs/NC, indicating enhanced redox kinetics and interfacial charge transfer. Additionally, the overlapping CV curves over five cycles (Fig. S6) highlight excellent electrochemical reversibility of the S@CoNi-DSACs/NC cathode. To further evaluate catalytic efficiency, Tafel slopes were extracted from CV fitting. For peak I, the slopes are 138.9, 86.9, 95.1, and 67.5 mV dec^{-1} for NC, Co-SACs/NC, Ni-SACs/NC, and CoNi-DSACs/NC, respectively (Fig. 3b), while for peak III they are 96.4, 87.6, 93.3, and 52.8 mV dec^{-1}, respectively (Fig. 3c). The lowest Tafel slopes for CoNi-DSACs/NC in both instances confirm its superior bidirectional catalytic activity. These synergistic effects clearly establish CoNi-DSACs/NC as a highly effective electrocatalyst for enhancing sulfur redox kinetics and stabilizing polysulfide conversion.

Electrochemical Impedance Spectroscopy (EIS) was employed to investigate the charge transfer kinetics of the cells, as represented by the semicircular feature in the Nyquist plot in Fig. S7. The Nyquist plots revealed a progressive decrease in charge transfer resistance (R_{ct}) from bare NC to the dual-atom catalyst. As shown in Fig. S7, the S@NC cathode exhibited the largest semicircle, indicative of poor electrical conductivity and sluggish interfacial electron transfer. Incorporation of Co or Ni single atoms into the NC matrix significantly reduced the R_{ct}, with Ni-SACs@NC outperforming Co-SACs@NC, likely due to more favorable electronic interactions between Ni atoms with higher d-electron density and the NC substrate, which facilitates faster electron transfer kinetics. Notably, S@CoNi-DSACs@NC cathode displayed the smallest semicircle among all cells, signifying the lowest R_{ct} and superior conductivity. This enhancement is attributed to the synergistic effect between Co and Ni atoms, which optimizes the electronic structure, facilitates faster charge transfer, and increases the density of catalytically active sites. Following 1000 GCD cycles in LSBs, EIS measurements demonstrated that all cathodes experienced an increase in R_{ct} (Fig. S8), likely due to interfacial degradation and active material loss. However, the extent of this increase varied significantly. Bare NC exhibited the most severe degradation, with a dramatic rise in R_{ct}, confirming its poor stability. Co-SACs@NC and Ni-SACs@NC showed moderate increases in resistance, with Ni-SACs maintaining better retention of their initial conductivity. In contrast, the CoNi-DSACs@NC cell retained the lowest R_{ct} even after prolonged cycling, highlighting its superior electrochemical stability and structural robustness under dynamic sulfur redox conditions. These

This journal is © The Royal Society of Chemistry 2025

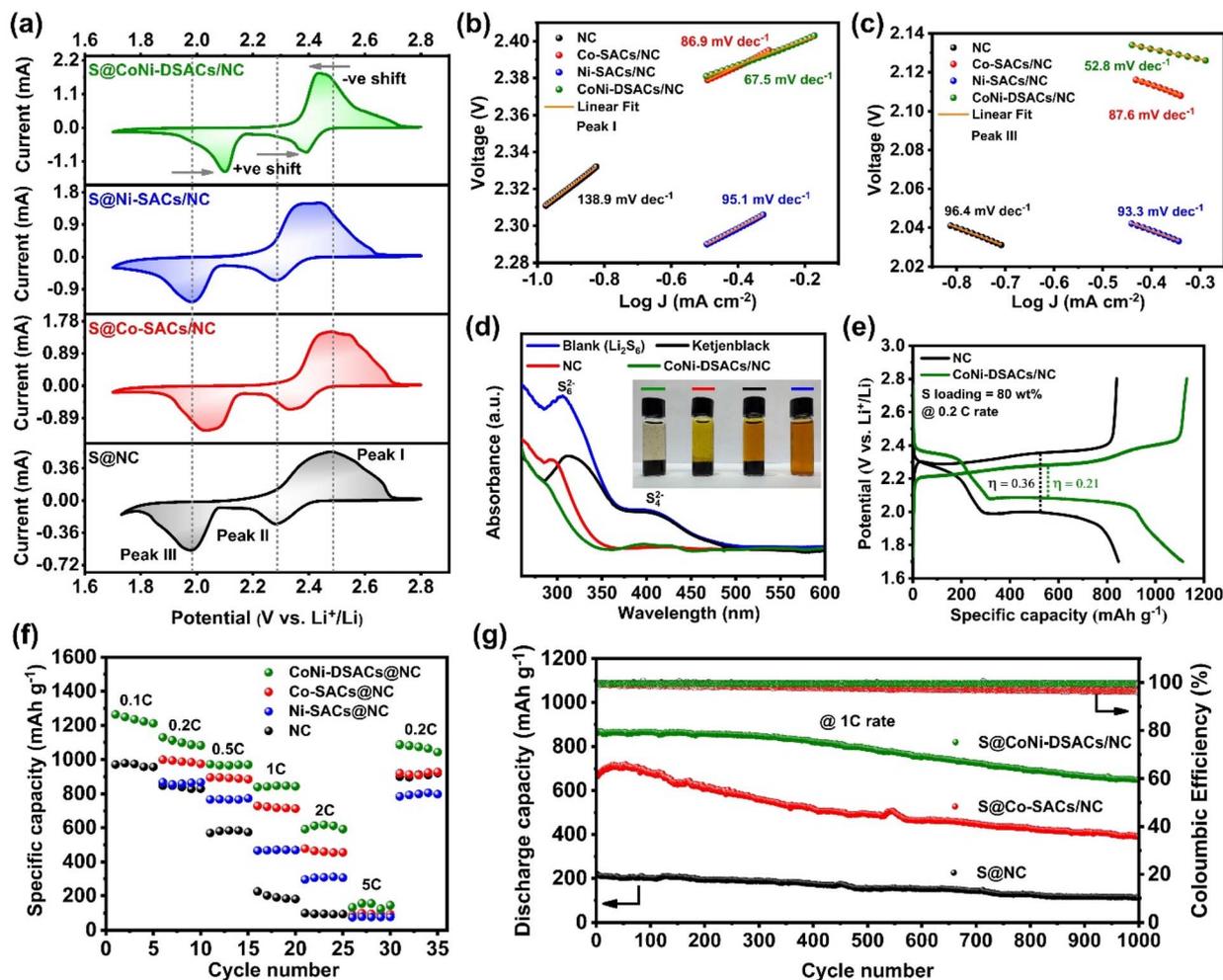*J. Mater. Chem. A*, 2025, **13**, 38421–38435 | **38425**

Fig. 3 Comparison of the electrochemical performance of LSBs using NC, SACs, and DSACs electrocatalytic sulfur hosts with S loading of 80 wt%. (a) Cyclic voltammetry (CV) at a scan rate of 0.1 mV s^{-1}. (b and c) Tafel plots for the redox reactions. (d) UV-vis spectra to monitor the adsorption strength of different sulfur hosts with Li$_2$S$_6$. (e) GCD cycle at 0.2C. (f) Discharge capacity at varied current rates (0.1–5 C) to evaluate the rate capability of the cast cathodes. (g) Long-term cycling stability at 1C rate.

findings reinforce the advantage of dual-metal coordination in sustaining both conductivity and catalytic activity over extended cycling in LSB applications.

The lithium-ion diffusion coefficient (D_{Li^+}) was calculated from the low-frequency region of the EIS spectra using the Warburg impedance model. The real part of the impedance (Z') was plotted against the inverse square root of angular frequency ($\omega^{-1/2}$), and the slope of the resulting linear region was used to extract the Warburg coefficient (σ), as shown in Fig. S9. The diffusion coefficient was then determined by the following formula:

$$D_{Li^+} = \frac{1}{2}\left(\frac{RT}{n^2 A F^2 \sigma C}\right)^2$$

where R is the gas constant (8.314 J mol^{-1} K^{-1}), T (298.5 K) is the absolute temperature, A is the electrode area (1.767 cm^2), n is the number of electrons transferred per molecule, F is Faraday's constant (96 485 C mol^{-1}), C is the molar concentration of lithium ions, and σ is the Warburg coefficient. As summarized

in Table S2, NC exhibited the lowest D_{Li^+}, indicating sluggish ion transport due to its limited electrochemical activity and poor conductivity. Ni-SACs@NC and Co-SACs@NC showed enhanced D_{Li^+} values due to more favorable lithium-ion adsorption and desorption kinetics. Remarkably, the CoNi-DSACs/NC cell demonstrated the highest D_{Li^+}, reflecting the optimized ion diffusion pathways facilitated by the dual-atom sites and their synergistic interaction with the NC matrix. These results are consistent with the observed EIS trends and further confirm the superior electrochemical performance of the CoNi-DSAC/NC electrocatalyst in LSBs configurations.

The adsorption of lithium polysulfides (Li$_2$S$_6$) is critical for mitigating the shuttle effect and improving LSB performance. To evaluate the adsorption capability of various hosts, UV-vis spectroscopy and optical imaging were used to monitor color changes in Li$_2$S$_6$ solutions (Fig. 3d and S10). Ketjenblack (KB) exhibited the weakest adsorption, as indicated by the persistent deep yellow solution and minimal decrease in absorbance, due to its nonpolar nature and lack of functional groups. In

38426 | J. Mater. Chem. A, 2025, 13, 38421–38435

This journal is © The Royal Society of Chemistry 2025

contrast, graphene oxide (GO) and NC showed moderate adsorption, attributed to their oxygen- and nitrogen-containing groups, which facilitated improved binding and solution fading. CoNi-DSACs/NC demonstrated significantly stronger Li_2S_6 adsorption, evidenced by nearly complete solution decolorization and the most pronounced reduction in UV-vis absorbance. The S 2p XPS spectra after Li_2S_6 adsorption highlight distinct binding environments on NC and CoNi-DSACs/NC (Fig. S11). For NC, two main contributions are observed: a component at ~162.2 eV, attributed to chemically adsorbed sulfide species (coordinated to N-doped sites), and a broader feature near 163.5 eV, assigned to intact polysulfide species physically adsorbed on the NC surface. This indicates that NC offers moderate chemical stabilization, though a substantial fraction of sulfur remains weakly bound. In contrast, CoNi-DSACs/NC exhibits an additional low-binding energy feature (~160.4 eV) corresponding to thiolate-like M–S bonds, confirming strong Lewis acid–base interactions at the Co/Ni single-atom sites. Together with the 162.1 eV contribution from coordinated sulfides, these chemically anchored species account for nearly half of the total sulfur, while only a minor fraction remains as physically adsorbed polysulfide (~163.5 eV). This dual binding pathway, M–S coordination at single-atom sites combined with N-doped carbon anchoring, establishes CoNi-DSACs/NC as a significantly stronger host for polysulfide immobilization than metal-free NC.

The galvanostatic charge–discharge (GCD) results of conventionally cast cathodes with an 80 wt% sulfur loading highlight the superior electrochemical performance and catalytic efficiency of S@CoNi-DSACs/NC toward LiPS conversion. Specifically, the S@CoNi-DSACs/NC cathode achieved a remarkable reversible capacity of 1115.9 mAh g^{-1} at 0.2C, outperforming the S@Co-SACs (989.7 mAh g^{-1}) and S@NC (847.5 mAh g^{-1}) cathodes, as illustrated in Fig. 3e and Fig. S12. As shown in Fig. 3e, the discharge plateaus of the S@CoNi-DSACs/NC cathode are flatter and more prolonged, exhibiting a lower polarization ($\eta = 0.21$ V) compared to those of S@NC ($\eta = 0.36$ V). This enhanced performance can be attributed to the synergistic catalytic activity of the dual single-atom Co and Ni sites, which facilitate more efficient LiPS adsorption and conversion, reducing capacity loss. The rate capability of the cathodes was further assessed using GCD measurements across a broad range of current densities (0.1–5.0C). As shown in Fig. 3f, S@CoNi-DSACs/NC consistently exhibited higher specific capacities than NC or mono-SACs/NC cathodes, demonstrating superior charge transfer kinetics during lithiation and delithiation. Notably, the S@CoNi-DSACs/NC cathode maintained a high capacity of 1264.2 mAh g^{-1} at 0.1C, with a gradual decrease to 1129.1, 974.8, 838.9, 612.5, and 149.3 mAh g^{-1} at 0.2, 0.5, 1, 2, and 5C, respectively. Importantly, upon reducing the current rate back to 0.2C, a reversible capacity of 1087.9 mAh g^{-1} was recovered, underscoring the electrode's excellent reversibility and minimal degradation. Furthermore, long-term cycling stability tests at 1C (Fig. 3g) demonstrated that the S@CoNi-DSACs/NC cathode retained outstanding structural integrity and electrochemical reversibility over 1000 cycles, exhibiting a minimal capacity decay rate

of only 0.024% per cycle, compared to the S@NC cathode with a decay rate of 0.048% per cycle.

Afterward, we conducted GCD tests on various cast S@CoNi-DSACs/NC cathodes with areal mass loadings ranging from 1.5 to 4.5 mg cm^{-2} to investigate the effect of cathode thickness on battery performance. The results shown in Fig. 4a demonstrated a noticeable decrease in capacity as the cathode thickness increased, suggesting a reduction in lithium-ion diffusion rates and limited sulfur utilization in the 2D cast cathodes. More specifically, the capacity of the LSB based on the cast S@CoNi-DSACs/NC cathode dropped from 1288.6 to 755.9 mAh g^{-1} (41% capacity loss) when the thickness of the cathode increased from 1.5 to 4.5 mg cm^{-2}. This indicates that the insufficient pathways for lithium ions mainly limit the battery's performance. It is worth noting that conventionally cast cathodes with high sulfur loading are prone to severe cracking.[43,44] Such cracks can weaken the structural integrity of the cathode, leading to increased susceptibility to mechanical degradation during repeated charging and discharging cycles. Moreover, these cracks create discontinuities in the cathode material, disrupting charge and ion-conductive pathways. This increases the internal resistance of the battery, resulting in lower power output and reduced efficiency.[45] Consequently, cracks may thus contribute to decreased battery performance, lower capacity, and a shorter lifespan. Additionally, ions and electrons transport through long and non-smooth paths within the dense coating, which fails to adequately accommodate volume fluctuations. As a result, 2D casted electrodes exhibit sluggish redox kinetics and low sulfur utilization at high areal loadings, especially under high current density conditions.

Based on the above findings, it is crucial to develop ink formulations and printing processes for fabricating 3D-printed cathodes using the DIW technique to establish effective ion pathways, minimize interfacial resistance, and accommodate the volumetric changes that occur within the structure during battery operation. By combining DIW with an electrocatalytic sulfur host tailored with a specific metal composition, we created sulfur cathodes with higher areal loading and enhanced electrolyte/cathode interfaces. Various electrode patterns can be easily, rapidly, and precisely produced using DIW (Fig. S13). The printing process involved three main stages: (1) ink formulation, (2) DIW, and (3) post-processing (freeze-drying), as described in Scheme 1. The interplay between ink formulation and printed patterns has a significant influence on battery performance and mechanical stability, ensuring structural integrity without compromising sulfur loading, catalytic activity, or the electrolyte/cathode ratio. For successful 3D printing, we formulated an ink consisting of PVDF (10 wt%) as a binder, NMP for dissolving the polymer and enhancing the layer-to-layer adhesion, KB (10 wt%) as a conductive additive, GO (10 wt%) for mechanical reinforcement, and S@CoNi-DSACs/NC (70 wt%) as the sulfur-based cathode material. To ensure optimal ink flow through the fine nozzle (250 μm) without clogging, the particle size of the mixture in the formulated ink must be sufficiently minimized. To achieve this, S@CoNi-DSACs/NC, GO, and KB were subjected to ball milling for 30 minutes. The resulting powder was then filtered through
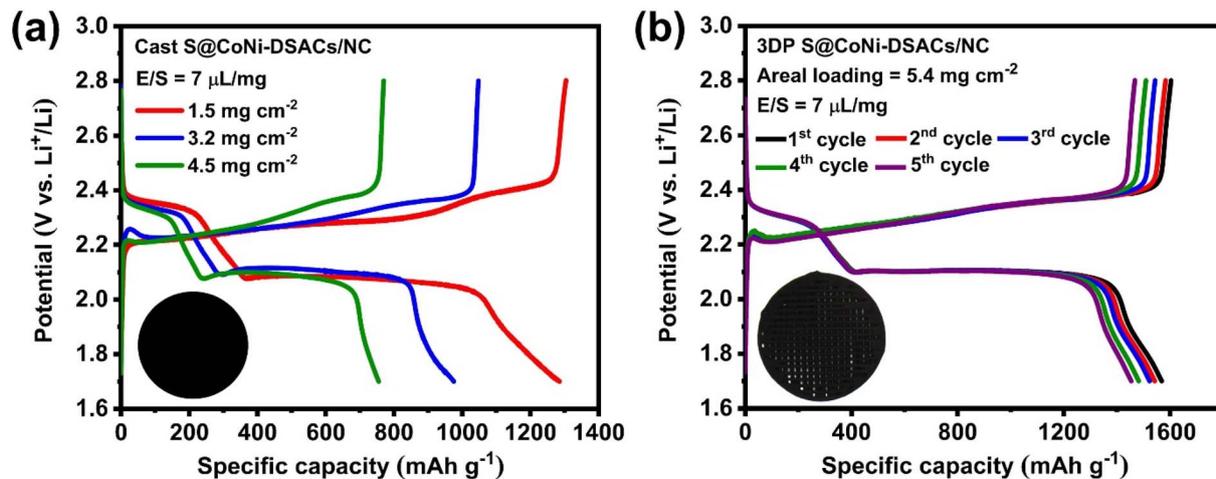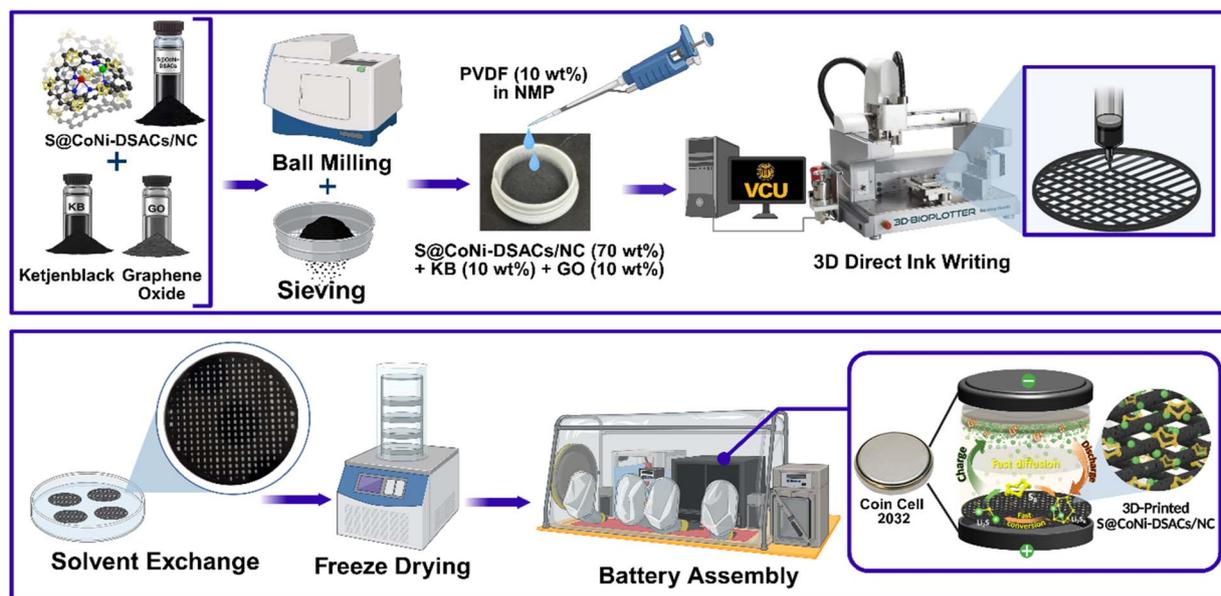
This journal is © The Royal Society of Chemistry 2025

J. Mater. Chem. A, 2025, 13, 38421–38435 | 38427

Fig. 4 (a) GCD profiles at 0.1C of (a) cast S@CoNi-DSACs/NC cathodes with various areal sulfur loadings (1.5–4.5 mg cm^{-2}) and (b) 3DP S@CoNi-DSACs/NC cathode with areal sulfur loading of 5.4 mg cm^{-2}. The inset is the optical image of (a) cast and (b) 3DP cathode.

Scheme 1 Schematic illustration of the DIW process for fabricating 3DP sulfur cathodes and the subsequent coin cell assembly.

a 50-micron sieve to achieve the desired particle size distribution. SEM images (Fig. 5a) demonstrate the size homogeneity of the ink material after ball milling.

The rheological characteristics of the ink were evaluated using a rheometer at 25 °C prior to the printing process. The viscosity data (Fig. S14a) reveal a peak viscosity of approximately 1000 Pa s. Notably, the ink exhibits shear-thinning behavior as the shear rate increases beyond this threshold. In addition, we characterized the storage modulus (G') and loss modulus (G'') of the formulated inks (Fig. S14b). The results indicate that the ink formulation maintains significantly elevated storage modulus ($\sim 10^5$ Pa) throughout the majority of the amplitude spectrum, suggesting that the ink behaves predominantly like a solid, an advantageous

property for successful 3D printing applications. Another critical step is degassing the ink to remove trapped air, which is essential for preventing bubble formation during printing. When the bubbles in the paste were not completely removed, they squeezed out instead of the paste during printing, forming intermittent lines. Therefore, the ink with optimized viscoelasticity was transferred to a 50 mL syringe and centrifuged at 2200 rpm for 5 minutes to eliminate air pockets, ensuring consistent extrusion. Post-processing involved placing the printed cathode in a freeze-dryer system, which operated at −80 °C and 0.5 mbar, to effectively evaporate the solvent while preserving grid integrity and promoting the formation of hierarchically porous structures. While NMP provided effective adhesion, enhancing the cross-linking of the
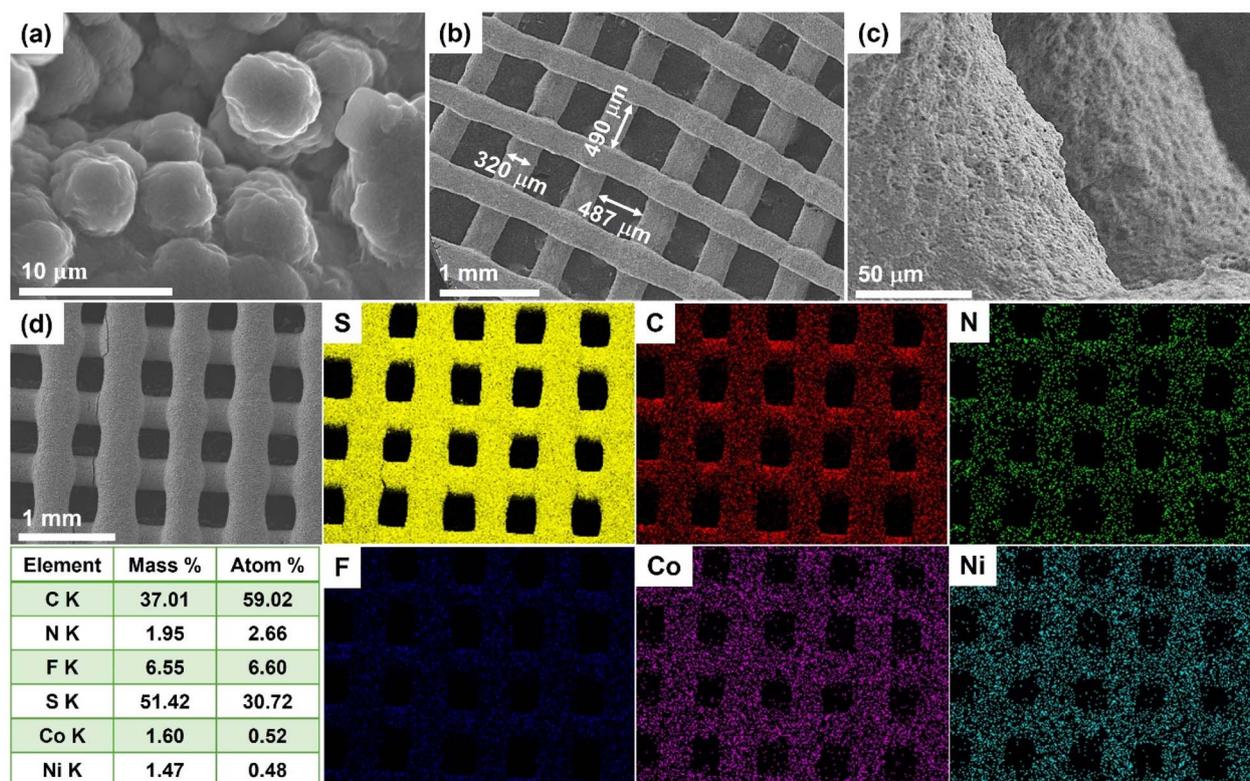
Fig. 5 (a) SEM image of ball-milled S@CoNi-DSACs/NC with KB and GO for ink formulation. (b and c) SEM images of the surface morphology of the 3DP S@CoNi-DSACs/NC cathodes indicate microporosity formation after freeze-drying the printed cathodes. (d) SEM-EDX images of the 3DP S@CoNi-DSACs/NC cathodes indicate homogeneous element distribution within the printed pattern.

binder and promoting adhesion between different printing layers, its high boiling point and low vapor pressure posed challenges, resulting in crack formation after freeze-drying (Fig. S15a–c). Additionally, the elevated toxicity of NMP presents environmental risks when scaling up the production of high-capacity batteries. To address these challenges, we explored phase inversion by replacing NMP with other solvents that have low boiling points and high vapor pressure to reduce crack formation. Ultimately, *t*-butanol proved to be the most effective solvent for substituting NMP before freeze-drying. It preserved the binder without compromising structural integrity, resulting in stable, free-standing cathodes (Fig. S16–18). Detailed procedures for tuning the DIW ink formulation, key printing parameters, and freeze-drying optimization are provided in the SI (Experimental methods) and summarized in Table S3.

SEM and EDX analyses (Fig. 5) elucidate the grid-like architecture of the 3D-printed S@CoNi-DSACs/NC cathodes following freeze-drying. The SEM images reveal a regular network of printed lines with an average diameter of ~320 μm and an interline spacing of ~490 μm, forming a well-defined square pore structure. This engineered macroporosity, combined with additional micropores introduced during freeze-drying, facilitates efficient ion transport and enables effective electrolyte infiltration at the macroscopic scale. Minimizing the spacing between adjacent printed lines is critical, as it directly

affects the gravimetric energy density and electrolyte wettability upon cell assembly. Fig. 5 and S18 display various printed cathodes showcasing different line spacings and printed layers. Remarkably, even after four printed layers, the intersecting lines exhibit seamless fusion, resembling a weld-like connection, thereby reinforcing the multidirectional electron transport pathways. Moreover, cross-sectional SEM imaging (Fig. S19a) confirms an average single-layer thickness of ~190 μm, while higher-magnification SEM and EDX elemental mapping (Fig. S19b and c) show that the ink-active materials are well-integrated and uniformly distributed within the structure. Elemental mapping (Fig. 5d) further demonstrates the homogeneous distribution of S, C, N, F, Co, and Ni within the 3D-printed matrix. The optical images from the Nikon digital microscope (Fig. S20) show top and side views of the first and second printed layers, which corroborate an average layer thickness of ~190–200 μm and demonstrate strong interlayer contact, contributing to an integrated conductive framework.

Coin-cell performance of the 3D-printed cathodes

DIW provides a promising route for fabricating high-energy-density LSBs, where sulfur loading can be readily increased by printing additional cathode layers (Fig. 6a). To evaluate the synergistic effects of 3D architecture and catalytic functionality, coin cells were assembled using 3D-printed S@CoNi-DSACs/NC cathodes. The GCD profiles (Fig. 4b and 6b) reveal superior
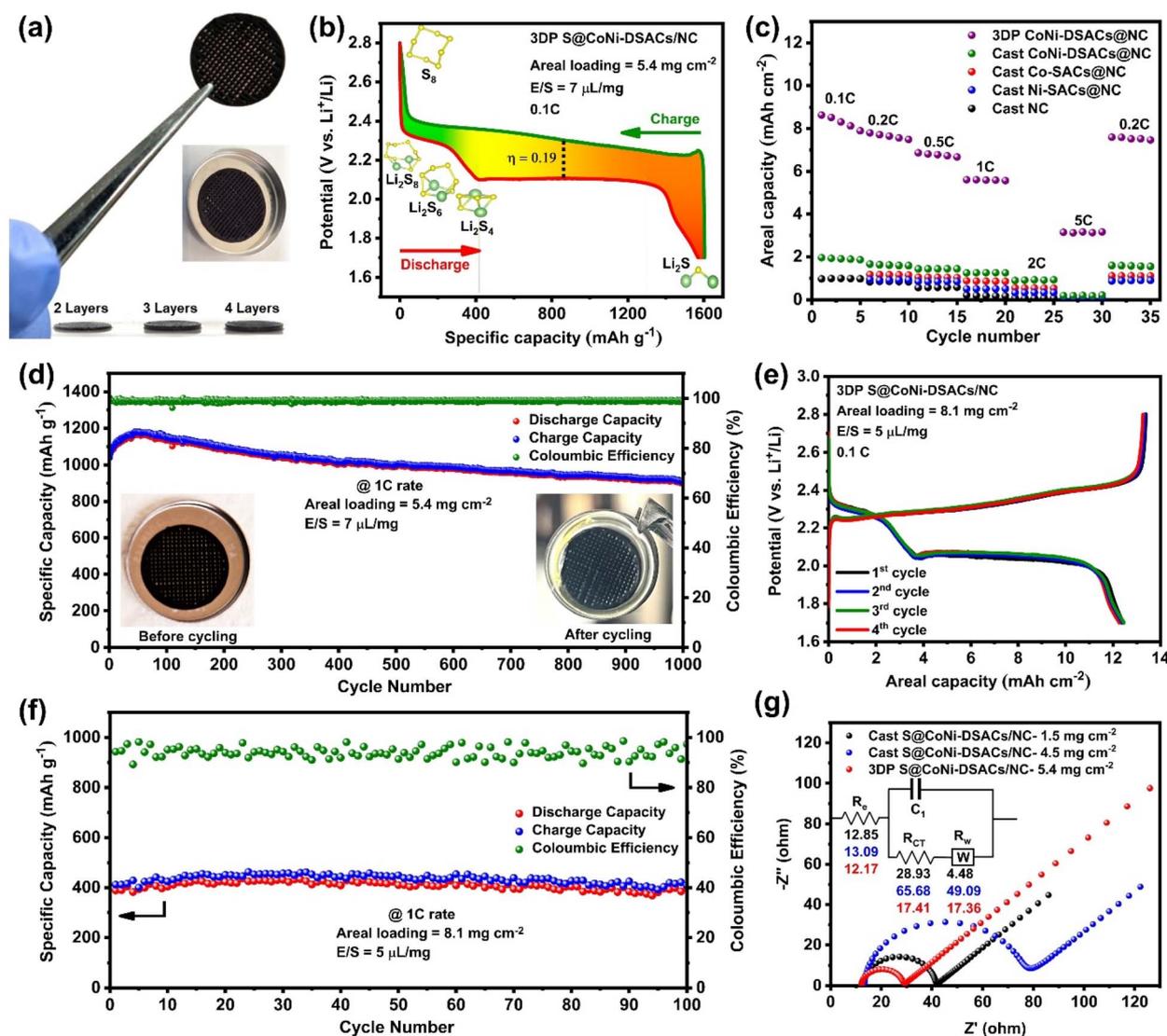
Fig. 6 (a) Optical images of free-standing cathodes demonstrate the high areal sulfur loadings of the 3D printed cathodes. (b) GCD profile of LSB using 3D printed S@CoNi-DSACs/NC cathode showing the kinetic rate at 0.1C. (c) Areal capacity of the sulfur-based electrocatalytic cathodes with different areal loadings (cast cathodes: 1–1.5 mg cm^{-2} while 3DP: 5.4 mg cm^{-2}). (d) Long-term cycling stability of the 3DP S@CoNi-DSACs/NC cathode at 1.0C rate for 1000 cycles. (e) Areal capacity and (f) stability of 3DP S@CoNi-DSACs/NC cathode with high areal sulfur loading of 8.1 mg cm^{-2}. EIS analysis of cast and 3DP cathodes with different areal loadings.

performance of the 3DP cathode, delivering 1567.3 mAh g^{-1} at 0.1C compared to 1264.2 mAh g^{-1} for the cast cathode. As illustrated in Fig. 6b, the observed charge/discharge characteristics featured two distinct plateaus near 2.37 V and 2.1 V, indicative of the conversion processes from solid elemental sulfur (S_8) to liquid polysulfides (Li_2S_8, Li_2S_6, and Li_2S_4), followed by their reduction to solid short-chain Li_2S_2 or Li_2S, aligning with the findings from CV analyses. Rate performance (Fig. 6c, Fig. S21) further underscores the advantage of the 3DP cathode over its cast counterpart at various current rates. The 3DP cathode exhibited remarkable kinetics during lithiation/delithiation, showing a capacity decline from 1567.3 mAh g^{-1} at 0.1C to 1452.7, 1274.2, 1039.2, 1047.6, and 596.2 mAh g^{-1} at 0.2, 0.5, 1, and 5C, respectively. Notably, when the current rate

was reverted from 5.0 to 0.2C, a recoverable reversible capacity of 1412.9 mAh g^{-1} was achieved, further underscoring the high reversibility and minimal capacity attenuation of the 3DP S@CoNi-DSACs/NC cathode. Importantly, the 3DP cathode (5.4 mg cm^{-2}) achieved an areal capacity of 8.46 mAh cm^{-2} at 0.1C, outperforming cast cathodes with lower loadings (1.0–1.5 mg cm^{-2}), as shown in Fig. 6c.

The cycling stability of LSBs employing the 3DP S@CoNi-DSACs/NC cathode is depicted in Fig. 6d. With a high sulfur loading of 5.4 mg cm^{-2}, the 3DP cathode demonstrated a remarkable initial discharge specific capacity of 1041.1 mAh g^{-1} at 1C and retained 890.6 mAh g^{-1} after 1000 cycles, corresponding to 85.5% capacity retention and an ultralow fade rate of 0.014% per cycle. In contrast, the cast S@CoNi-DSACs/NC

38430 | J. Mater. Chem. A, 2025, 13, 38421–38435

This journal is © The Royal Society of Chemistry 2025

cathode presented earlier (Fig. 3g) showed a diminished discharge capacity of 648.9 mAh g^{-1} after 1000 cycles, corresponding to a retention rate of 73.1%. The optical images of the disassembled 3DP cathode after cycling (Fig. S22) reveal a preserved lattice structure, confirming its outstanding mechanical robustness during cycling. Even when the sulfur loading increased to 8.1 mg cm^{-2}, the 3DP cathode displayed an outstanding discharge specific (areal) capacity of 1538.4 mAh g^{-1} (12.5 mAh cm^{-2}) at 0.1C, as shown in Fig. 6e and S23. Over 100 cycles at 1C under lean electrolyte conditions (E/S = 5 μL mg^{-1}), it maintained 91.1% capacity retention with a maximum discharge capacity of 436.5 mAh g^{-1} (Fig. 6f). These metrics clearly outperform most previously reported cast and 3DP sulfur cathodes (Table S4), which often face trade-offs between high sulfur loading and stable areal capacity.[46–50] Unlike many prior hosts that compromise between sulfur loading and areal capacity, our work integrates Co/Ni dual-site SACs with DIW-fabricated, current-collector-free 3D architectures to simultaneously achieve high sulfur loading, high areal capacity, and excellent cycling stability. As a proof of concept, the assembled 3DP LSB successfully powered 21 LED lights (Fig. S24), underscoring its potential for practical application.

EIS was further employed to evaluate the charge transfer and ion diffusion behavior of cast and 3DP S@CoNi-DSACs/NC cathodes with varying areal sulfur loadings. As shown in Fig. 6g, increasing the sulfur loading of the cast cathode from 1.5 to 4.5 mg cm^{-2} results in a pronounced enlargement of the semicircle in the Nyquist plot, corresponding to a substantial increase in charge transfer resistance (R_{ct}). This deterioration is primarily attributed to hindered electrolyte infiltration and reduced accessibility of conductive pathways within the thickened electrode. Moreover, the Warburg region of the Nyquist plot (Fig. S25) reveals a shallower slope for the cast cathode, indicating slower Li$^+$ diffusion kinetics. To quantify this effect, the real part of impedance (Z') was plotted against the inverse square root of angular frequency ($\omega^{-1/2}$), and the Warburg coefficient (σ) was extracted from the slope. The cast cathode (4.5 mg cm^{-2}) exhibited a higher Warburg coefficient (σ = 49.09), corresponding to a lower Li$^+$ diffusion coefficient (D_{Li^+}). In contrast, the 3DP cathode, despite having a higher sulfur loading of 5.4 mg cm^{-2}, showed a significantly smaller semicircle and a steeper low-frequency tail, indicating lower R_{ct} and faster diffusion. The Warburg coefficient for the 3DP cathode was substantially lower (σ = 17.37), reflecting improved Li$^+$ transport. This enhanced electrochemical performance is attributed to the architected porous structure enabled by 3D printing, which promotes efficient electrolyte penetration, continuous ion diffusion pathways, and faster polysulfide redox kinetics. These findings, summarized in Table S2, demonstrate that structural optimization *via* additive manufacturing can effectively overcome the traditional trade-off between high areal loading and interfacial transport limitations in LSBs.

Building upon the enhanced charge transfer, improved Li$^+$ diffusion, and high areal sulfur loading enabled by the 3D printing strategy, the underlying adsorption-conversion mechanism in the 3DP S@CoNi-DSACs/NC cathode arises from synergistic interplay between architecture and chemistry, as

illustrated in Fig. 7a. The hierarchically porous, printed NC scaffold ensures fast electronic/ionic transport, as well as uniform electrolyte infiltration. Meanwhile, atomically dispersed Co–N$_x$ and Ni–N$_x$ motifs act as spatially proximate, chemically distinct active sites that lower activation barriers throughout the polysulfide redox cycle. The S 2p spectrum after Li$_2$S$_6$ adsorption over CoNi-DSACs/NC displays low-binding-energy M–S features, indicating direct metal–sulfur interactions that promote Li$_2$S nucleation during discharge and facilitate Li$_2$S decomposition during charge. Mechanistically, Co–N$_x$ sites provide strong adsorption and favor electron-driven reduction pathways toward Li$_2$S formation (improving nucleation and capacity utilization), whereas Ni–N$_x$ sites facilitate the oxidation/decomposition steps (Li$_2$S $\rightarrow$ polysulfide $\rightarrow$ S$_8$) during charging, accelerating polysulfide redox kinetics and improving reversibility, as systematically proved by the CV and kinetic analyses. The intimate electronic coupling between Co–N$_x$ and Ni–N$_x$ motifs within the conductive NC network balances adsorption strength and desorption/catalysis, reducing polarization and enhancing rate capability.

Post-mortem XPS, XRD, SEM/EDX, and X-CT analyses (Fig. 7b–d, S26 and S27) confirm the dynamic evolution of sulfur species and the catalytic role of the designed active sites, while the printed architecture accommodates volume change and sustains long-term cycling stability. The interactions between CoNi-DSACs/NC catalyst and lithium polysulfides (LiPS) were systematically examined to evaluate their role in mitigating LiPS migration, using X-ray photoelectron spectroscopy (XPS) for comprehensive analysis. XPS measurements were performed on both pristine and cycled cathodes to capture the evolution of sulfur species during battery operation. Prior to cycling, the high-resolution XPS spectrum of the S 2p region exhibited characteristic doublet peaks attributed to elemental sulfur (S$_8$) at binding energies of 164.3 eV (S 2p$_{3/2}$) and 165.4 eV (S 2p$_{1/2}$), as depicted in Fig. 7b.[11,51] These peaks serve as a baseline for tracking sulfur transformations during subsequent charge–discharge processes. After 50 cycles, the fully discharged coin cell was disassembled in an argon-filled glovebox, and the S@CoNi-DSACs/NC cathode was extracted for post-mortem analysis. A significant alteration in the S 2p spectrum was observed, marked by the disappearance of the S$_8$ peaks and the emergence of distinct signals corresponding to short-chain polysulfides. Specifically, binding energy peaks at 161.5 eV and 160.2 eV were attributed to lithium sulfide (Li$_2$S$_2$) and lithium disulfide (Li$_2$S), respectively.[52] These observations confirm the effective conversion of long-chain polysulfides into short-chain counterparts, indicative of favorable polysulfide redox kinetics facilitated by the CoNi-DSACs/NC catalyst. Notably, a minor residual peak at 163.1 eV suggested the presence of a limited amount of long-chain polysulfides (Li$_2$x; x > 2). Additionally, the broad peaks between 167.0 eV and 170.4 eV, associated with thiosulfate (SO$_3^{2-}$) and polythionate complexes, showed a marked reduction in intensity compared to the charged state. This decline indicates the effective suppression of intermediate sulfur species and highlights the catalytic role of CoNi-DSACs/NC in accelerating the polysulfide conversion process. Further insights were gained by analyzing the S@CoNi-
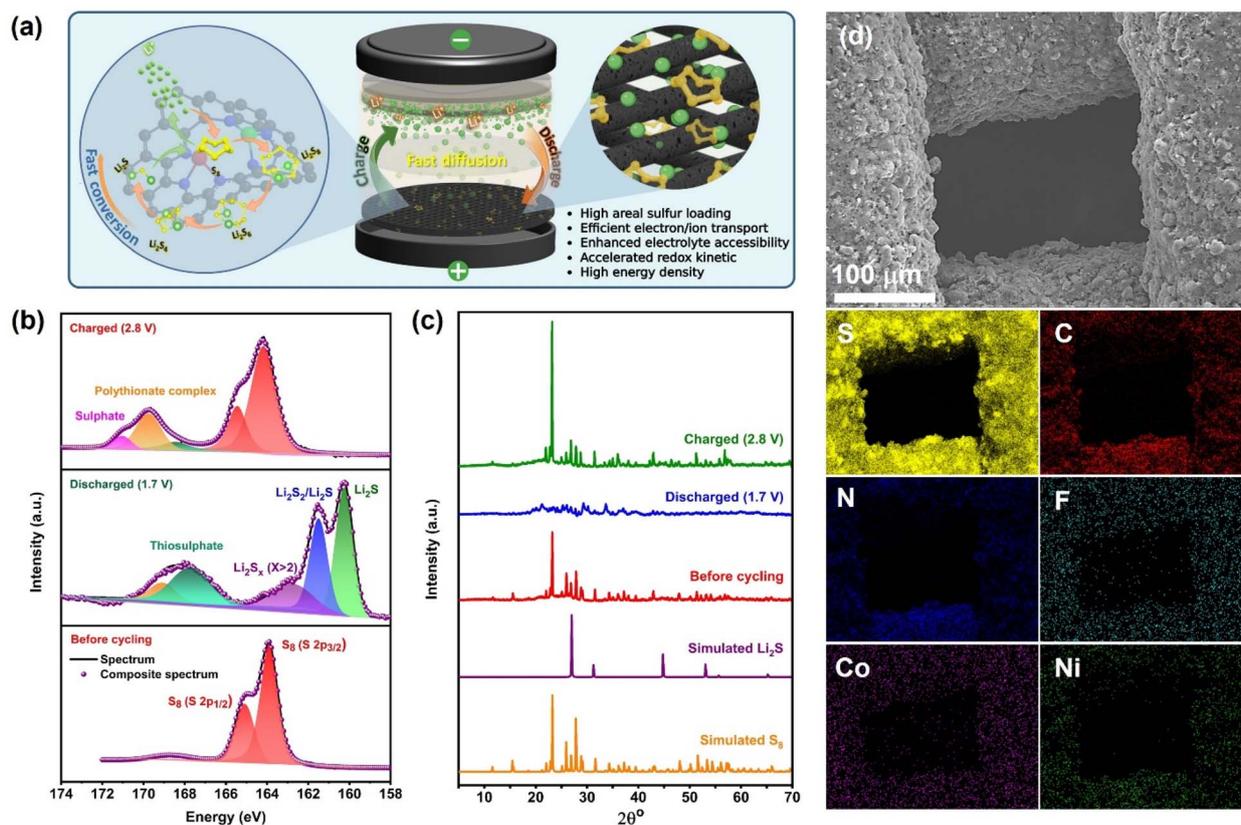
This journal is © The Royal Society of Chemistry 2025

J. Mater. Chem. A, 2025, 13, 38421–38435 | 38431

Fig. 7 (a) Schematic representation highlights the rapid lithium-ion diffusion and the conversion mechanism in the 3DP S@CoNi-DSACs/NC cathode arises from synergistic interplay between architecture and chemistry. (b) High-resolution XPS and (c) PXRD of the 3DP S@CoNi-DSACs/NC cathode before and after cycling (discharged/charged for 50 cycles). (d) SEM-EDX images of the charged 3DP S@CoNi-DSACs/NC cathodes after 1000 cycles indicate preserved macroscopic/microscopic pore architecture and homogeneous element distribution within the printed pattern.

DSACs/NC cathode extracted from a fully charged cell. The S 2p spectrum prominently featured peaks at 164.1 eV and 165.4 eV, corresponding to the reformation of elemental sulfur (S_8), confirming the reversible conversion of Li_2S back to sulfur during charging. The appearance of additional peaks at 167.3 eV, 169.1 eV, and 170.4 eV suggested the formation of sulfur-related byproducts such as thiosulfate, polythionate complexes, and sulfate species, respectively, coupled with the suppression of soluble intermediates, elucidates the robust interactions between CoNi-DSACs/NC and LiPS.[52]

XRD analysis was also performed to investigate the structural evolution of the 3DP S@CoNi-DSACs/NC cathode before and after cycling (Fig. 7c). The pristine cathode exhibited distinct diffraction peaks at $2\theta \approx 23°$ and 28°, corresponding to the (222) and (440) planes of crystalline orthorhombic sulfur (S_8). After 50 GCD cycles, the XRD pattern of the fully discharged state showed the disappearance of these characteristic sulfur peaks, indicating the formation of amorphous lithium sulfide (Li_2S) as the final reduction product. Conversely, upon full charging, the reappearance of sulfur diffraction peaks confirmed the reversible conversion of Li_2S back to crystalline S_8. The observed higher S_8 peak intensity in the fully charged state compared to the pristine cathode indicates improved

sulfur crystallinity and redistribution, driven by CoNi-DSACs catalyst. Collectively, this efficient S_8–Li_2S reversibility underscores the catalyst's capability to accelerate the sulfur redox process while mitigating the shuttle effect. To this end, we demonstrate that combining DIW with a strategically engineered electrocatalytic sulfur host enables the design of high areal cathodes with exceptional areal capacity.

Post-mortem SEM/EDX (Fig. 7d and S26) and X-ray computed tomography (X-CT, Fig. S27) analyses after 1000 cycles confirm the structural and chemical resilience of the 3D-printed CoNi-DSACs/NC cathode. SEM reveals that the printed grid geometry is retained, indicating robust resistance to sulfur redox-induced volume changes. Meanwhile, EDX mapping shows a uniform sulfur distribution and persistent co-localization of Co and Ni, consistent with stable dual-metal single-atom sites under prolonged cycling. The observed F signal is attributable to the PVDF binder, and N dopants remain detectable, suggesting preservation of the metal-nitrogen coordination environment. Quantitative composition from EDX and 3D reconstructed X-CT of the 3DP cathodes (before and after cycling) further corroborates material retention: the designed electrode composition is largely maintained, and internal porosity increases only modestly from 18.6% to 22.0%, over

38432 | J. Mater. Chem. A, 2025, **13**, 38421–38435

This journal is © The Royal Society of Chemistry 2025

1000 cycles. Together, these data indicate that the engineered 3D architecture accommodates volumetric changes without large-scale fracture or pore collapse, thereby preserving electrolyte access and continuous ion/electron pathways that underpin the demonstrated long-term electrochemical stability of the 3DP CoNi-DSACs/NC cathode.

Realizing device-relevant performance from Li–S cathodes requires a rigorous balance of sulfur loading, porosity, and ion transport; the 3D-printed S@CoNi-DSACs/NC grids provide a model platform where this balance can be systematically quantified and optimized. Increasing sulfur areal loading yields dramatic practical gains: the two-layer 3DP grid (5.40 mg cm^{-2}; E/S = 7 µL mg^{-1} S) delivers 8.46 mAh cm^{-2} with 93.6% sulfur utilization (N/P ~9.3), and the three-layer grid (8.10 mg cm^{-2}; E/S = 5 µL mg^{-1} S) delivers 12.50 mAh cm^{-2} with 91.8% utilization (N/P ~6.3), *versus* the cast control (1.50 mg cm^{-2}) at 1.99 mAh cm^{-2} and 76.9% utilization (N/P = 39.4) (Table S5; SI Experimental methods). These improvements reflect more complete active-material utilization and a substantial reduction in practical Li excess afforded by thicker, high-loading printed electrodes. The volumetric consequences are more nuanced and expose the central design trade-off. SEM and X-CT indicate a single printed layer thickness of ~190 µm and internal porosity φ ~18.6%, giving stack thicknesses of 0.0380 cm (two layers) and 0.0570 cm (three layers). Accounting for the grid packing density (f_{xy} = 0.653, based on a line diameter of 320 µm and spacing of 490 µm), the effective volumetric grid capacities are 341 mAh cm^{-3} and 336 mAh cm^{-3} for the two- and three-layer 3DP cathodes, respectively. When normalized to the solid fraction, the values further rise to 419 mAh cm^{-3} and 413 mAh cm^{-3} (Table S5; step-by-step calculations are provided in the SI). These data reveal the inherent trade-off in thick, porous electrodes: while stacking layers increases areal capacity and lowers N/P, additional geometric thickness and macroporosity limit volumetric scaling by lengthening ion-transport pathways and increasing mass-transport polarization.

Increasing the areal capacity and reducing the electrolyte to sulfur ratio (E/S) are critical to attaining ultrahigh energy density LSBs.[53] This trend is clearly demonstrated in the present study (Fig. S28), where comparative performance metrics of cast and 3DP S@CoNi-DSACs/NC cathodes at varying sulfur areal loadings highlight the superior capability of the 3D-printed architecture under practical cell conditions. Based on coin-cell calculations, the 8.1 mg cm^{-2} cathode yields 19.24 mAh per cell and an internal gravimetric energy of 311.95 Wh kg^{-1}, whereas full-coin metrics are limited by casing and inactive components (14.80 Wh kg^{-1}, 40.19 Wh L^{-1}). All key electrochemical metrics are reported in Table S5, and step-by-step calculations are provided in the SI (Experimental method). Taken together, these results demonstrate that DIW 3DP cathodes enable high areal energy and efficient lithium utilization while explicitly exposing macrostructural limitations. Translating these gains into volumetrically competitive devices requires targeted design strategies, including reduced interline spacing, graded porosity, ion-conductive fillers or gel interlayers, and conductive scaffold integration, all compatible with DIW processing and accessible for future optimization.[54,55]

It is worth noting that while DIW affords exceptional geometric control over 3D electrode architectures, translating these advantages to practical cells remains a challenge. 3D DIW throughput remains lower than that of conventional slurry casting methods, and printed electrodes may experience mechanical instability when compressed in full cells. Possible scale-up paths to address these barriers include multi-nozzle or continuous printing platforms, polymer/composite reinforcement of printed filaments, and the development of greener or water-based ink formulations that simplify drying and handling.[56,57] Extending the use of DIW cathodes to solid-state LSBs introduces additional interfacial constraints limiting the effective cathode/electrolyte interface. Mitigation approaches, including *in situ* polymer infiltration, tailored soft interlayers, and pressure-assisted assembly (*e.g.*, controlled hot-pressing), can promote intimate electrode–electrolyte contact and preserve the advantages of architected cathodes.[56,58–60] With these promising engineering solutions, DIW stands as a unique fabrication technique to advance LSBs performance using both liquid and solid electrolytes.

Conclusion

This study demonstrates a DIW strategy to overcome the low practical energy density of cast LSBs by fabricating free-standing, architecturally precise S@CoNi-DSACs/NC cathodes. The 3D-printed design integrates ordered micro/macroporosity with dual Co/Ni single-atom sites, enabling efficient ion/electron transport, effective polysulfide regulation, and accelerated redox kinetics. At a sulfur loading of 5.4 mg cm^{-2}, the cathode delivers 1041.4 mAh g^{-1} at 1C with an ultralow decay rate of 0.014% over 1000 cycles. Even when the sulfur loading increased to 8.1 mg cm^{-2}, the 3DP cathode achieves 1538.4 mAh g^{-1} (12.5 mAh cm^{-2}) at 0.1C, highlighting its suitability for practical high-loading applications. Post-mortem SEM/EDX and X-CT confirm the retention of grid geometry, uniform Co/Ni dispersion, preserved N coordination, and only a modest increase in porosity (18.6% to 22.0%) after 1000 cycles, indicating outstanding structural robustness. These results establish 3D printing of SACs-integrated N-doped carbon frameworks as a powerful and versatile platform for designing durable, high-loading Li–S cathodes and provide a versatile platform for next-generation conversion-type energy storage systems.

Conflicts of interest

The authors declare no competing financial interest.

Data availability

The data supporting this article have been included as part of the supplementary information (SI). Supplementary information: experimental methods; Fig. S1–S28; Table S1–S5; additional information on battery electrochemical measurements; characterization of cast film cathodes and 3D printed cathodes. See DOI: **https://doi.org/10.1039/d5ta06211j**.

This journal is © The Royal Society of Chemistry 2025

J. Mater. Chem. A, 2025, **13**, 38421–38435 | **38433**

Acknowledgements

References

1 X. Shen, D. Shen, J. Zhu and X. Duan, *Adv. Funct. Mater.*, 2025, 1–36.

2 T. Liang, X. Zhang, Y. Huang, Y. Lu, H. Jia, Y. Yuan, L. Meng, Y. Zhou, L. Zhou, P. Guan, T. Wan, M. Ferry and D. Chu, *Small*, 2024, 1–20.

3 Z. Xu, J. Chen, T. Zhang, H. Lu, L. Yan, J. Ning and Y. Hu, *Adv. Energy Mater.*, 2024, 1–14.

4 X. Y. Liu, S. Li, Y. F. Zhu, X. Y. Zhang, Y. Su, M. Y. Li, H. W. Li, B. B. Chen, Y. F. Liu and Y. Xiao, *Adv. Funct. Mater.*, 2024, 1–41.

5 P. Zeng, B. Su, X. Wang, X. Li, C. Yuan, G. Liu, K. Dai, J. Mao, D. Chao, Q. Wang and L. Zhang, *Adv. Funct. Mater.*, 2023, **33**, 1–17.

6 C. Sun, J. Zhu, B. Liu, M. Xu, J. Jiang and T. Yu, *ACS Energy Lett.*, 2023, **8**, 772–779.

7 L. Zhou, D. L. Danilov, R. A. Eichel and P. H. L. Notten, *Adv. Energy Mater.*, 2021, **11**, 2001304.

8 W. Yao, J. Xu, L. Ma, X. Lu, D. Luo, J. Qian, L. Zhan, I. Manke, C. Yang, P. Adelhelm and R. Chen, *Adv. Mater.*, 2023, **35**, 1–49.

9 J. Lei, T. Liu, J. Chen, M. Zheng, Q. Zhang, B. Mao and Q. Dong, *Chem*, 2020, **6**, 2533–2557.

10 C. Zhou, C. Dong, W. Wang, Y. Tian, C. Shen, K. Yan, L. Mai and X. Xu, *Interdiscip. Mater.*, 2024, **3**, 306–315.

11 M. M. Kaid, M. K. Shehab, H. Fang, A. I. Ahmed, S. A. El-Hakam, A. A. Ibrahim, P. Jena and H. M. El-Kaderi, *ACS Appl. Mater. Interfaces*, 2024, **16**, 2283–2295.

12 Y. Zhang, C. Kang, W. Zhao, Y. Song, J. Zhu, H. Huo, Y. Ma, C. Du, P. Zuo, S. Lou and G. Yin, *J. Am. Chem. Soc.*, 2023, **145**, 1728–1739.

13 T. Zhou, J. Liang, S. Ye, Q. Zhang and J. Liu, *Energy Stor. Mater.*, 2023, **55**, 322–355.

14 C. Dong, C. Ma, C. Zhou, Y. Yu, J. Wang, K. Yu, C. Shen, J. Gu, K. Yan, A. Zheng, M. Gong, X. Xu and L. Mai, *Adv. Mater.*, 2024, **36**, 1–12.

15 P. Rao, X. Han, H. Sun, F. Wang, Y. Liang, J. Li, D. Wu, X. Shi, Z. Kang, Z. Miao, P. Deng and X. Tian, *Angew. Chem., Int. Ed.*, 2025, **137**, e202415223.

16 Y. Liu, Y. Qing, W. Jiang, L. Zhou, C. Chen, L. Shen, B. Li, M. Zhou and H. Lin, *Small*, 2024, 1–26.

17 J. Chen, M. R. Ahasan, J. S. Oh, J. A. Tan, S. Hennessey, M. M. Kaid, H. M. El-Kaderi, L. Zhou, K. U. Lao, R. Wang and W. N. Wang, *J. Mater. Chem. A*, 2024, **12**, 4601–4609.

18 X. Xia, J. Yang, Y. Liu, J. Zhang, J. Shang, B. Liu, S. Li and W. Li, *Adv. Sci.*, 2023, **10**, 1–23.

19 Y. Mu, Y. Chu, L. Pan, B. Wu, L. Zou, J. He, M. Han, T. Zhao and L. Zeng, *Int. J. Extreme Manuf.*, 2023, **5**, 042008.

20 J. Li, J. Fleetwood, W. B. Hawley and W. Kays, *Chem. Rev.*, 2022, **122**, 903–956.

21 C. Liu, X. Cheng, B. Li, Z. Chen, S. Mi and C. Lao, *Materials*, 2017, **10**, 934.

22 L. Zeng, S. Ling, D. Du, H. He, X. Li and C. Zhang, *Adv. Sci.*, 2023, **10**, 1–26.

23 C. H. Hung, P. Huynh, K. Teo and C. L. Cobb, *ACS Energy Lett.*, 2023, **8**, 296–305.

24 C. Chen, J. Jiang, W. He, W. Lei, Q. Hao and X. Zhang, *Adv. Funct. Mater.*, 2020, **30**, 1–7.

25 S. Zhou, I. Usman, Y. Wang and A. Pan, *Energy Stor. Mater.*, 2021, **38**, 141–156.

26 X. Liu, J. Wang, B. Wu, H. Li, P. Ma and H. Y. Yang, *Adv. Funct. Mater.*, 2025, 1–29.

27 X. Hai, S. Xi, S. Mitchell, K. Harrath, H. Xu, D. F. Akl, D. Kong, J. Li, Z. Li, T. Sun, H. Yang, Y. Cui, C. Su, X. Zhao, J. Li, J. Pérez-Ramírez and J. Lu, *Nat. Nanotechnol.*, 2022, **17**, 174–181.

28 J. Gu, Z. Shi, T. Yan, M. Tian, Z. Chen, S. Chen, Y. Ding, M. Lu, Y. Zou, J. Zhang, L. Zhang and J. Sun, *Small*, 2024, 1–10.

29 S. Choudhary, N. Oli, S. Shweta, S. Kumar, M. K. Bhattarai, C. A. Malca-Reyes, R. K. Katiyar, B. Tripathi, L. M. Díaz-Vázquez, G. Morell and R. S. Katiyar, *Molecules*, 2024, **29**, 1–18.

30 J. Xu, K. Tao, Y. Zhu, T. Zhou, X. Huang, J. Li and J. Liu, *Chem. Commun.*, 2025, **61**, 2345–2348.

31 J. He, A. Bhargav and A. Manthiram, *ACS Nano*, 2021, **15**(5), 8583–8591.

32 M. M. Rahman, A. Z. Shafiullah, A. Pal, M. A. Islam, I. Jahan and B. B. Saha, *Energies*, 2021, **14**(22), 7478.

33 S. Gamal, D. A. Kospa, M. M. Kaid, S. A. El-Hakam, A. I. Ahmed and A. A. Ibrahim, *J. Environ. Chem. Eng.*, 2023, **11**, 109359.

34 R. Diab, G. Boltaev, M. M. Kaid, A. Fawad, H. M. El-Kaderi, M. H. Al-Sayah, A. S. Alnaser and O. M. El-Kadri, *Sci. Rep.*, 2025, **15**, 3682.

35 A. A. Ibrahim, M. M. Kaid, S. L. Ali, S. E. Samra, S. A. El-Hakam and A. I. Ahmed, *Inorg. Chem. Commun.*, 2023, **153**, 110748.

36 M. M. Kaid, O. Elbanna, S. A. El-Hakam, H. M. El-Kaderi and A. A. Ibrahim, *J. Photochem. Photobiol., A*, 2022, **430**, 114001.

37 A. Alzharani, M. K. Shehab, D. D. Rodene, J. U. Ahmed, A. M. Bakry, M. M. Kaid and H. M. El-Kaderi, *Energy Fuels*, 2022, **36**, 4967–4977.

38434 | *J. Mater. Chem. A*, 2025, **13**, 38421–38435

This journal is © The Royal Society of Chemistry 2025

38 M. Kim, D. H. Nam, H. Y. Park, C. Kwon, K. Eom, S. Yoo, J. Jang, H. J. Kim, E. Cho and H. Kwon, *J. Mater. Chem. A*, 2015, **3**, 14284–14290.

39 Y. Zhou, Q. Zhou, H. Liu, W. Xu, Z. Wang, S. Qiao, H. Ding, D. Chen, J. Zhu, Z. Qi, X. Wu, Q. He and L. Song, *Nat. Commun.*, 2023, **14**, 3776.

40 S. Gul, F. Nasim, M. A. Nadeem, M. Imran, A. Waseem and M. A. Nadeem, *Electrochim. Acta*, 2025, **514**, 145575.

41 M. M. Kaid, E. Kaplan, C. Weththasingha, A. Nag, N. Norouzi, H. M. El-Kaderi and K. M. Tibbetts, *ACS Appl. Energy Mater.*, 2025, **8**(1), 227–237.

42 M. K. Shehab, M. M. Kaid, S. Pokhrel, O. K. Farha and H. M. El-kaderi, *ACS Appl. Energy Mater.*, 2025, **8**(17), 12651–12660.

43 J. Lee, M. S. Oh, S. Kim, I. Kim, K. N. Jung, M. H. Ryu, G. Doo, J. Jung, S. G. Im and H. T. Kim, *Commun. Mater.*, 2025, **6**, 1–8.

44 D. Lv, J. Zheng, Q. Li, X. Xie, S. Ferrara, Z. Nie, L. B. Mehdi, N. D. Browning, J. G. Zhang, G. L. Graff, J. Liu and J. Xiao, *Adv. Energy Mater.*, 2015, **5**, 1–8.

45 K. F. Ye, Y. P. Xia, R. Li, B. H. Liu and Z. P. Li, *Electrochim. Acta*, 2022, **435**, 141387.

46 P. Wang, Z. Zhang, X. Yan, M. Xu, Y. Chen, J. Li, J. Li, K. Zhang and Y. Lai, *J. Mater. Chem. A*, 2018, **6**, 14178–14187.

47 J. Zhang, Z. Xie, W. Xi, Y. Zhang, R. Wang, Y. Gong, B. He, H. Wang and J. Jin, *Adv. Energy Mater.*, 2024, 1–11.

48 Y. Ouyang, W. Zong, X. Zhu, L. Mo, G. Chao, W. Fan, F. Lai, Y. E. Miao, T. Liu and Y. Yu, *Adv. Sci.*, 2022, **9**, 1–11.

49 Z. Shi, Z. Sun, J. Cai, Z. Fan, J. Jin, M. Wang and J. Sun, *Adv. Funct. Mater.*, 2021, **31**, 1–9.

50 X. Gao, Q. Sun, X. Yang, J. Liang, A. Koo, W. Li, J. Liang, J. Wang, R. Li, F. B. Holness, A. D. Price, S. Yang, T. K. Sham and X. Sun, *Nano Energy*, 2019, **56**, 595–603.

51 M. G. Rabbani, R. K. Sasse, S. Behera, P. Jena, J. Liu, P. K. Thallapally, T. Islamoglu, M. K. Shehab, M. M. Kaid, O. K. Farha and H. M. El-Kaderi, *Langmuir*, 2024, **40**, 8024–8034.

52 X. Liang, C. Hart, Q. Pang, A. Garsuch, T. Weiss and L. F. Nazar, *Nat. Commun.*, 2015, **6**, 5682.

53 G. Zhou, H. Chen and Y. Cui, *Nat. Energy*, 2022, **7**, 312–319.

54 S. Mooraj, Z. Qi, C. Zhu, J. Ren, S. Peng, L. Liu, S. Zhang, S. Feng, F. Kong, Y. Liu, E. B. Duoss, S. Baker and W. Chen, *Nano Res.*, 2021, **14**, 2105–2132.

55 C. Zhu, N. B. Schorr, Z. Qi, B. R. Wygant, D. E. Turney, G. G. Yadav, M. A. Worsley, E. B. Duoss, S. Banerjee, E. D. Spoerke, A. van Buuren and T. N. Lambert, *Small Struct.*, 2023, **4**, 2200323.

56 F. W. Yang, Y. J. Shen, Z. P. Zhang, W. H. Ruan, M. Z. Rong and M. Q. Zhang, *Adv. Mater.*, 2025, 1–13.

57 L. Zhou, W. Ning, C. Wu, D. Zhang, W. Wei, J. Ma, C. Li and L. Chen, *Adv. Mater. Technol.*, 2019, **4**, 1–7.

58 F. Pei, L. Wu, Y. Zhang, Y. Liao, Q. Kang, Y. Han, H. Zhang, Y. Shen, H. Xu, Z. Li and Y. Huang, *Nat. Commun.*, 2024, **15**, 1–10.

59 W. Lyu, H. Fu, A. M. Rao, Z. Lu, X. Yu, Y. Lin, J. Zhou and B. Lu, *Sci. Adv.*, 2024, **10**, 1–12.

60 W. Lee, J. Lee, T. Yu, H. J. Kim, M. K. Kim, S. Jang, J. Kim, Y. J. Han, S. Choi, S. Choi, T. H. Kim, S. H. Park, W. Jin, G. Song, D. H. Seo, S. K. Jung and J. Kim, *Nat. Commun.*, 2024, **15**, 5860.

This journal is © The Royal Society of Chemistry 2025

J. Mater. Chem. A, 2025, **13**, 38421–38435 | **38435**